



## A 4-node hybrid stress-function (HS-F) plane element with drilling degrees of freedom less sensitive to severe mesh distortions

Song Cen<sup>a,c</sup>, Ming-Jue Zhou<sup>a</sup>, Xiang-Rong Fu<sup>b,\*</sup>

<sup>a</sup> Department of Engineering Mechanics, School of Aerospace, Tsinghua University, Beijing 100084, China

<sup>b</sup> College of Water Conservancy and Civil Engineering, China Agricultural University, Beijing 100083, China

<sup>c</sup> AML, School of Aerospace, Tsinghua University, Beijing 100084, China

### ARTICLE INFO

#### Article history:

Received 15 June 2010

Accepted 14 December 2010

Available online 12 January 2011

#### Keywords:

Finite element

Hybrid stress-function (HS-F) element

Drilling degree of freedom

Fundamental analytical solutions

Severe mesh distortions

### ABSTRACT

A simple but robust 4-node hybrid stress-function (HS-F) membrane element with drilling degrees of freedom is developed based on the principle of minimum complementary energy. Its stress fields are derived from the first seven fundamental analytical solutions of the Airy stress function. The assumed displacements along element boundaries employ compatible mode of Allman for which the nodal drilling degrees of freedom are considered. Numerical results show that the proposed new element, denoted as HSF-Q40-7 $\beta$ , exhibits much improved numerical accuracy and robust performance. In particular, the element performs well even when the element shape degenerates into a triangle or concave quadrangle.

© 2010 Elsevier Ltd. All rights reserved.

### 1. Introduction

The quadrilateral and hexahedral isoparametric finite elements are the most popular models used in various numerical analyses. However, once the element shape is distorted, its numerical accuracy may deteriorate dramatically, or even the analysis process has to be stopped [1,2]. Recently, a number of techniques are still being proposed for developing new high-performance finite element models which are robust and less sensitive to mesh distortions; these include, for examples, the quadrilateral area and hexahedral volume coordinate method [3–11], the unsymmetric interpolation element method [12–15], the new spline finite element method [16,17], the Alpha finite element method [18]. Of course, one should also remember that, during the history of the finite element development [2], there are many other effective techniques have been systematically developed to overcome the difficulties caused by various mesh distortions, such as the use of incompatible modes [19–26], and so on.

The idea of introducing drilling degrees of freedom at each node of a plane element is not new. Indeed, it can improve the order of the element displacement fields, thus to enhance the element performance without increasing the number of element nodes. Moreover, such drilling degrees of freedom in membrane (plane stress) elements possess special significance for the finite element analysis of shells. That is, a membrane element with drilling degrees of

freedom can be combined with a plate bending element to form a flat-shell element, for which the problem of singular coefficients associated with the degrees of freedom in the direction normal to the plane of the shell element can be naturally alleviated. Numerous researches on plane elements with drilling degrees of freedom have been accomplished since the mid-60s. A remarkable scheme was previously proposed by Allman [27], who introduced a quadratic displacement approximation to supplement the drilling degrees of freedom at element nodes. Bergan and Fellipa [28] proposed a free formulation method considering drilling degrees of freedom. Cook [29] combined a hybrid method with the drilling degrees of freedom. MacNeal and Harder [30] refined Allman's element to remove spurious modes and locking due to Poisson effects. Element formulations based on the modified variational principles with independent approximation of the rotational field were given by Hughes and Brezzi [31], Ibrahimbegovic et al. [32], Iura and Atluri [33]. Cazzani and Atluri [34] presented a few 4-node assumed unsymmetric stress membrane elements. Long and Xu [35,36] suggested a new definition of vertex rigid drilling degree of freedom and developed corresponding generalized conforming element models. Piltner and Taylor [37] considered three sets of enhanced strain functions for the improvement of the three-node triangular finite elements with rotational degrees of freedom. Geyer and Groenwold [38] formulated two membrane element families with drilling degrees of freedom by hybrid stress technique and Hu–Washizu like functional. Pimpinelli [39] proposed an assumed strain quadrilateral element based on the minimization of the modified Hu–Washizu functional where the enhanced

\* Corresponding author.

E-mail address: [fuXR99@mails.tsinghua.edu.cn](mailto:fuXR99@mails.tsinghua.edu.cn) (X.-R. Fu).

strain and the enhanced rotation fields are included. Groenwold et al. [40] also designed new hybrid stress elements based on direct enforcement of traction free condition through manipulation of the elemental assumed stress field. Choi et al. [41,42] proposed hybrid Trefftz plane elements with drilling degrees of freedom. Zhang and Kuang [43] presented an 8-node membrane element with drilling degrees of freedom for analysis of in-plane stiffness of thick floor plates. Other new developments of the membrane elements with drilling degrees of freedom can be found in most recent papers [44,45].

Recently, by improving Pian's first version hybrid stress element method [46], Fu et al. [47] and Cen et al. [48] proposed a hybrid stress-function element method for developing plane elements. The strategy of these new formulations is as follows: (1) instead of assuming stress fields directly, the Airy stress function  $\phi$ , treated as a functional variable, is introduced into the complementary energy functional, (2) the analytical solution of  $\phi$  is found to be the trial functions for the 2D elements, and the corresponding unknown stress-function constants are introduced; by doing so, the stresses satisfy both the equilibrium and compatibility conditions, (3) using the principle of minimum complementary energy, the unknown stress-function constants can be expressed in terms of the displacements along element boundaries, which are, in turn, interpolated by the element nodal displacements, (4) finally, the complementary energy functional can be rewritten in terms of element nodal displacement vector, and thus, the element stiffness matrix of such hybrid stress-function (HS-F) element is obtained. The resulting 8-node and 12-node quadrilateral plane elements can produce the exact solutions for pure bending and linear bending problems, respectively, even when the elements degenerate into triangles or concave quadrangles. Moreover, these elements do not possess any spurious modes, nor show any rotational frame dependence.

By following the strategy outlined in the above, a 4-node plane quadrilateral element with drilling degrees of freedom is presented in this paper. The element stress fields are derived from the fundamental analytical solutions of the Airy stress function, and possess first order completeness in Cartesian coordinates  $x$  and  $y$ . And the element boundary displacements employ quadratic displacement field with the drilling degrees of freedom along an edge suggested by Allman [27]. To assess the numerical performance of the proposed formulation, a number of benchmark problems are solved using the new element and the results are compared with other known 4-node quadrilateral elements available in the literatures. It clearly shows that the present element exhibits better numerical accuracy and improved convergence property for both stresses and displacements. In particular, the element can still perform well even when the element shape degenerates into a triangle or concave quadrangle. Furthermore, the element does not possess rotational frame dependence.

## 2. The general formulations of the hybrid stress-function element

Derivation procedure of the hybrid stress-function elements has been given in [47,48], thus will not be repeated herein. Only the major steps are outlined. For a plane finite element model, its complementary energy functional can be written in the following matrix form [46]:

$$\Pi_C = \Pi_C^* + V_C^* = \frac{1}{2} \iint_{A^e} \boldsymbol{\sigma}^T \mathbf{C} \boldsymbol{\sigma} t dA - \int_{\Gamma^e} \mathbf{T}^T \bar{\mathbf{u}} t ds \quad (1)$$

With

$$\Pi_C^* = \frac{1}{2} \iint_{A^e} \boldsymbol{\sigma}^T \mathbf{C} \boldsymbol{\sigma} t dA, \quad V_C^* = - \int_{\Gamma^e} \mathbf{T}^T \bar{\mathbf{u}} t ds, \quad (2)$$

$$\boldsymbol{\sigma} = \begin{Bmatrix} \sigma_x \\ \sigma_y \\ \tau_{xy} \end{Bmatrix}, \quad \mathbf{C} = \frac{1}{E} \begin{bmatrix} 1 & -\mu' & 0 \\ -\mu' & 1 & 0 \\ 0 & 0 & 2(1+\mu') \end{bmatrix}, \quad (3)$$

$$\mathbf{T} = \begin{Bmatrix} T_x \\ T_y \end{Bmatrix}, \quad \bar{\mathbf{u}} = \begin{Bmatrix} \bar{u} \\ \bar{v} \end{Bmatrix},$$

where  $\Pi_C^*$  is the complementary energy within the element;  $V_C^*$  is the complementary energy along the kinematic boundaries (here, all element boundaries are treated as the kinematic boundaries because the boundary displacements will be prescribed in Eq. (4));  $t$  is the thickness of the element;  $\boldsymbol{\sigma}$ , the element stress vector;  $\mathbf{T}$ , the surface force vector along the element boundaries;  $\mathbf{C}$ , the elastic flexibility matrix; also  $E' = E$  and  $\mu' = \mu$  for plane stress problem, whereas  $E' = E/(1 - \mu^2)$  and  $\mu' = \mu/(1 - \mu)$  for plane strain problem, in which  $E$  and  $\mu$  are Young's modulus and Poisson's ratio, respectively;  $\bar{\mathbf{u}}$ , the displacement vector along element boundaries, which can be interpolated by the element nodal displacement vector  $\mathbf{q}^e$ :

$$\bar{\mathbf{u}} = \mathbf{N}|_r \mathbf{q}^e, \quad (4)$$

where matrix  $\mathbf{N}|_r$  is the interpolation function matrix for element boundary displacements, and will be given in Section 3.

Following the usual procedure in the theory of elasticity, the stress vector  $\boldsymbol{\sigma}$  is derivable from the Airy stress function  $\phi$ , i.e.

$$\boldsymbol{\sigma} = \begin{Bmatrix} \sigma_x \\ \sigma_y \\ \tau_{xy} \end{Bmatrix} = \begin{Bmatrix} \frac{\partial^2 \phi}{\partial y^2} \\ \frac{\partial^2 \phi}{\partial x^2} \\ -\frac{\partial^2 \phi}{\partial x \partial y} \end{Bmatrix} = \tilde{\mathbf{R}}(\phi); \quad (5)$$

and the traction force vector  $\mathbf{T}$  can be written as

$$\mathbf{T} = \begin{Bmatrix} T_x \\ T_y \end{Bmatrix} = \begin{bmatrix} l & 0 & m \\ 0 & m & l \end{bmatrix} \begin{Bmatrix} \sigma_x \\ \sigma_y \\ \tau_{xy} \end{Bmatrix} = \mathbf{L} \tilde{\mathbf{R}}(\phi) \quad \text{with } \mathbf{L} = \begin{bmatrix} l & 0 & m \\ 0 & m & l \end{bmatrix}, \quad (6)$$

where  $l$  and  $m$  are the direction cosines of the outer normal  $n$  of the element boundaries.

Substitution Eqs. (5) and (6) into Eq. (1) yields

$$\Pi_C = \Pi_C^* + V_C^* = \frac{1}{2} \iint_{A^e} \tilde{\mathbf{R}}(\phi)^T \mathbf{C} \tilde{\mathbf{R}}(\phi) t dA - \int_{\Gamma^e} [\mathbf{L} \tilde{\mathbf{R}}(\phi)]^T \bar{\mathbf{u}} t ds \quad (7)$$

where

$$\Pi_C^* = \frac{1}{2} \iint_{A^e} \tilde{\mathbf{R}}(\phi)^T \mathbf{C} \tilde{\mathbf{R}}(\phi) t dA, \quad (8)$$

$$V_C^* = - \int_{\Gamma^e} [\mathbf{L} \tilde{\mathbf{R}}(\phi)]^T \bar{\mathbf{u}} t ds. \quad (9)$$

Thus, the element complementary energy functional containing the Airy stress function is established.

Let

$$\phi = \sum_{i=1}^N \phi_i \beta_i = \boldsymbol{\varphi} \boldsymbol{\beta}, \quad (10)$$

with

$$\boldsymbol{\varphi} = [\phi_1 \quad \phi_2 \quad \phi_3 \quad \cdots \quad \phi_N], \quad (11)$$

$$\boldsymbol{\beta} = [\beta_1 \quad \beta_2 \quad \beta_3 \quad \cdots \quad \beta_N]^T,$$

where  $N$  is the number of the fundamental analytical solutions used for stress function  $\phi$  in Eq. (10);  $\beta_i$  ( $i = 1-N$ ),  $N$  unknown constants;  $\phi_i$  ( $i = 1-N$ ),  $N$  fundamental analytical solutions (in Cartesian coordinates) of the Airy stress function  $\phi$ , which satisfy the following biharmonic equation (compatibility equation):

$$\nabla^4 \phi_i = \frac{\partial^4 \phi_i}{\partial x^4} + 2 \frac{\partial^4 \phi_i}{\partial x^2 \partial y^2} + \frac{\partial^4 \phi_i}{\partial y^4} = 0. \tag{12}$$

The first seven fundamental analytical solutions of  $\phi_i$  and resulting stresses are listed in Table 1. Obviously, such trial functions will directly lead to more reasonable stress fields satisfying both equilibrium and compatibility conditions.

Substitution of Eq. (10) into Eq. (8) yields

$$\Pi_C^* = \frac{1}{2} \boldsymbol{\beta}^T \mathbf{M} \boldsymbol{\beta} \tag{13}$$

with

$$\mathbf{M} = \iint_{A^e} \mathbf{S}^T \mathbf{C} \mathbf{S} t dA, \tag{14}$$

where  $\mathbf{M}$  is the flexibility matrix, and its evaluation procedure is given in the Appendix;  $\mathbf{S}$  is the stress solution matrix derived from Eqs. (5) and (10), given by

$$\mathbf{S} = \begin{bmatrix} \sigma_{x1} & \sigma_{x2} & \sigma_{x3} & \cdots & \sigma_{xN} \\ \sigma_{y1} & \sigma_{y2} & \sigma_{y3} & \cdots & \sigma_{yN} \\ \tau_{xy1} & \tau_{xy2} & \tau_{xy3} & \cdots & \tau_{xyN} \end{bmatrix}, \tag{15}$$

in which, stresses  $\sigma_{xi}$ ,  $\sigma_{yi}$  and  $\tau_{xyi}$  ( $i = 1-N$ ) are derived from the fundamental analytical solutions of  $\phi_i$  and their first seven expressions are given in Table 1.

Further, substitution of Eqs. (4) and (10) into Eq. (9) yields

$$V_C^* = -\boldsymbol{\beta}^T \mathbf{H} \mathbf{q}^e \tag{16}$$

with

$$\mathbf{H} = \int_{\Gamma} \mathbf{S}^T \mathbf{L}^T \mathbf{N}|_{\Gamma} t ds, \tag{17}$$

where  $\mathbf{H}$  is the leverage matrix, and its evaluation procedure is also given in the Appendix.

Then, after substituting Eqs. (13) and (16) into Eq. (7), the element complementary energy functional can be rewritten as

$$\Pi_C = \frac{1}{2} \boldsymbol{\beta}^T \mathbf{M} \boldsymbol{\beta} - \boldsymbol{\beta}^T \mathbf{H} \mathbf{q}^e. \tag{18}$$

According to the principle of minimum complementary energy, we require

$$\frac{\partial \Pi_C}{\partial \boldsymbol{\beta}} = \mathbf{0}. \tag{19}$$

Thus, by substituting Eq. (18) into Eq. (19), the unknown constant vector  $\boldsymbol{\beta}$  can be expressed in terms of the nodal displacement vector  $\mathbf{q}^e$ :

$$\boldsymbol{\beta} = \mathbf{M}^{-1} \mathbf{H} \mathbf{q}^e. \tag{20}$$

Substitution of Eq. (20) into Eq. (13) yields

$$\Pi_C^* = \frac{1}{2} \mathbf{q}^{eT} \mathbf{K}^* \mathbf{q}^e, \tag{21}$$

where

$$\mathbf{K}^* = (\mathbf{M}^{-1} \mathbf{H})^T \mathbf{H} = \mathbf{H}^T \mathbf{M}^{-1} \mathbf{H}. \tag{22}$$

**Table 1**  
The first seven fundamental analytical solutions of the Airy stress function and resulting stress solutions for plane problem.

| $i$           | 1     | 2    | 3     | 4     | 5      | 6      | 7     |
|---------------|-------|------|-------|-------|--------|--------|-------|
| $\phi_i$      | $x^2$ | $xy$ | $y^2$ | $x^3$ | $x^2y$ | $xy^2$ | $y^3$ |
| $\sigma_{xi}$ | 0     | 0    | 2     | 0     | 0      | 2x     | 6y    |
| $\sigma_{yi}$ | 2     | 0    | 0     | 6x    | 2y     | 0      | 0     |
| $\tau_{xyi}$  | 0     | -1   | 0     | 0     | -2x    | -2y    | 0     |

From the viewpoint of element definition given in [46], matrix  $\mathbf{K}^*$  in the above equation is considered as the stiffness matrix of the hybrid stress-function element. Since the form of the matrix  $\mathbf{K}^*$  is similar to those of the displacement-based elements, it can therefore be readily incorporated into a standard finite element program framework.

Once the element nodal displacement vector  $\mathbf{q}^e$  is found, the element stresses can be calculated from

$$\boldsymbol{\sigma} = \mathbf{S} \mathbf{M}^{-1} \mathbf{H} \mathbf{q}^e. \tag{23}$$

The stresses at any point can be readily evaluated by substituting the Cartesian coordinates of this point within an element into  $\mathbf{S}$  in the above equation, and then, the resulting strains can be obtained by the constitutive equations.

The determination procedure of the nodal equivalent load vector  $\mathbf{R}^e$  is similar with the usual schemes for displacement-based elements.

### 3. A new 4-node quadrilateral hybrid stress-function element with drilling degrees of freedom

Consider a 4-node quadrilateral element with drilling degree of freedom shown in Fig. 1,  $(\xi_i, \eta_i)$  and  $(x_i, y_i)$  ( $i = 1-4$ ) are the usual isoparametric and Cartesian coordinates of element nodes, respectively. Differing from the usual displacement-based models, the element shape is allowed to be either convex or concave.

For the 4-node elements with drilling degrees of freedom, the element nodal displacement vector  $\mathbf{q}^e$  is defined as

$$\mathbf{q}^e = [u_1 \quad v_1 \quad \theta_{z1} \quad u_2 \quad v_2 \quad \theta_{z2} \quad u_3 \quad v_3 \quad \theta_{z3} \quad u_4 \quad v_4 \quad \theta_{z4}]^T, \tag{24}$$

where  $u_i$ , and  $v_i$  ( $i = 1-4$ ) are the nodal displacements in  $x$ - and  $y$ -directions, respectively;  $\theta_{zi}$  ( $i = 1-4$ ) are the element nodal rotations. However, it should be noted that  $\theta_{zi}$  ( $i = 1-4$ ) are not the physical rotations of the element nodes. Instead, the definitions of the drilling degrees of freedom given by Allman [27] are employed.

According to the element displacement fields of Allman [27], the element boundary displacements can be written as [41]

$$\bar{\mathbf{u}} = \left\{ \begin{matrix} \bar{u} \\ \bar{v} \end{matrix} \right\} = \mathbf{N}|_{\Gamma} \mathbf{q}^e, \tag{25}$$

where

(i) for edge  $\bar{12}$  ( $\eta = -1$ )

$$\mathbf{N}|_{\bar{12}} = \begin{bmatrix} \bar{N}_1 & 0 & \bar{N}_{u\theta 1} & \bar{N}_2 & 0 & \bar{N}_{u\theta 2} & 0 & 0 & 0 & 0 & 0 & 0 \\ 0 & \bar{N}_1 & \bar{N}_{v\theta 1} & 0 & \bar{N}_2 & \bar{N}_{v\theta 2} & 0 & 0 & 0 & 0 & 0 & 0 \end{bmatrix}_{\bar{12}} \tag{26a}$$

$$\bar{N}_1 = \frac{1}{2}(1 - \xi), \quad \bar{N}_2 = \frac{1}{2}(1 + \xi),$$

$$\bar{N}_{u\theta 1} = \frac{y_1 - y_2}{8}(1 - \xi^2), \quad \bar{N}_{v\theta 1} = \frac{x_2 - x_1}{8}(1 - \xi^2),$$

$$\bar{N}_{u\theta 2} = -\bar{N}_{u\theta 1}, \quad \bar{N}_{v\theta 2} = -\bar{N}_{v\theta 1};$$

(ii) for edge  $\bar{23}$  ( $\xi = 1$ )

$$\mathbf{N}|_{\bar{23}} = \begin{bmatrix} 0 & 0 & 0 & \bar{N}_2 & 0 & \bar{N}_{u\theta 2} & \bar{N}_3 & 0 & \bar{N}_{u\theta 3} & 0 & 0 & 0 \\ 0 & 0 & 0 & 0 & \bar{N}_2 & \bar{N}_{v\theta 2} & 0 & \bar{N}_3 & \bar{N}_{v\theta 3} & 0 & 0 & 0 \end{bmatrix}_{\bar{23}}, \tag{26b}$$

$$\bar{N}_2 = \frac{1}{2}(1 - \eta), \quad \bar{N}_3 = \frac{1}{2}(1 + \eta),$$

$$\bar{N}_{u\theta 2} = \frac{y_2 - y_3}{8}(1 - \eta^2), \quad \bar{N}_{v\theta 2} = \frac{x_3 - x_2}{8}(1 - \eta^2), \quad \bar{N}_{u\theta 3} = -\bar{N}_{u\theta 2},$$

$$\bar{N}_{v\theta 3} = -\bar{N}_{v\theta 2};$$

(i) for edge  $\bar{34}$  ( $\eta = 1$ )

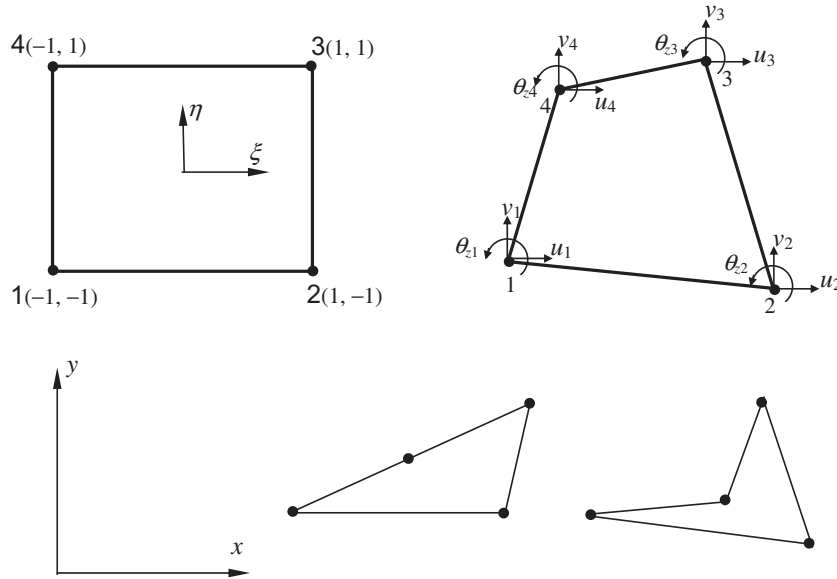


Fig. 1. 4-node hybrid stress-function quadrilateral plane element with drilling degrees of freedom.

$$\mathbf{N}|_{34} = \begin{bmatrix} 0 & 0 & 0 & 0 & 0 & 0 & \bar{N}_3 & 0 & \bar{N}_{u\theta 3} & \bar{N}_4 & 0 & \bar{N}_{u\theta 4} \\ 0 & 0 & 0 & 0 & 0 & 0 & 0 & \bar{N}_3 & \bar{N}_{v\theta 3} & 0 & \bar{N}_4 & \bar{N}_{v\theta 4} \end{bmatrix}_{34},$$

$$\bar{N}_3 = \frac{1}{2}(1 + \xi), \quad \bar{N}_4 = \frac{1}{2}(1 - \xi),$$

$$\bar{N}_{u\theta 3} = \frac{y_3 - y_4}{8}(1 - \xi^2), \quad \bar{N}_{v\theta 3} = \frac{x_4 - x_3}{8}(1 - \xi^2), \quad \bar{N}_{u\theta 4} = -\bar{N}_{u\theta 3},$$

$$\bar{N}_{v\theta 4} = -\bar{N}_{v\theta 3};$$

(26c)

(ii) for edge  $\bar{41}$  ( $\xi = -1$ )

$$\bar{\mathbf{N}}|_{41} = \begin{bmatrix} \bar{N}_1 & 0 & \bar{N}_{u\theta 1} & 0 & 0 & 0 & 0 & 0 & 0 & 0 & \bar{N}_4 & 0 & \bar{N}_{u\theta 4} \\ 0 & \bar{N}_1 & \bar{N}_{v\theta 1} & 0 & 0 & 0 & 0 & 0 & 0 & 0 & \bar{N}_4 & \bar{N}_{v\theta 4} \end{bmatrix}_{41},$$

$$\bar{N}_4 = \frac{1}{2}(1 + \eta), \quad \bar{N}_1 = \frac{1}{2}(1 - \eta),$$

$$\bar{N}_{u\theta 4} = \frac{y_4 - y_1}{8}(1 - \eta^2), \quad \bar{N}_{v\theta 4} = \frac{x_1 - x_4}{8}(1 - \eta^2), \quad \bar{N}_{u\theta 1} = -\bar{N}_{u\theta 4},$$

$$\bar{N}_{v\theta 1} = -\bar{N}_{v\theta 4};$$

(26d)

For matrix  $\mathbf{S}$  defined in Eq. (15), let  $N = 7$ , i.e., the first seven analytical solutions  $\phi_i$  ( $i = 1-7$ ) for the stress function  $\phi$  (see Eq. (10)), which have been listed in Table 1, are taken as the trial functions. That is to say, seven unknown constants  $\beta_i$  are introduced (see Eq. (11)). Then, the matrix  $\mathbf{S}$  in Eq. (15) is a  $3 \times 7$  matrix. It can be seen that the stress fields possess linear completeness in both  $x$  and  $y$ . The resulting element model is denoted as **HSF-Q40-7 $\beta$** .

It should be noted that, since the element boundary displacements are assumed independently, a spurious mode may occur for constant values of nodal rotations. If it occurs, such spurious mode only affects the results of the nodal rotations. Nevertheless, in reality so long as any appropriate constraints are imposed on one or more degrees of rotation, the spurious mode for rotations will vanish automatically.

#### 4. Numerical examples

Eight problems are used to evaluate and test the performance of the new element, and the results are compared against those obtained by using well-known or previously published elements. These elements are listed below:

- Q4: conventional 4-node bilinear isoparametric element with full integration scheme.
- QM6: 4-node nonconforming isoparametric element with internal parameters, Taylor et al. [50].
- QUAD4: 4-node quadrilateral element in MSC/NASTRAN, MacNeal et al. [49].
- P-S: 4-node quadrilateral hybrid-stress element, Pian et al. [51].
- Q4S: 4-node quadrilateral element with drilling DOFs, MacNeal et al. [30].
- GQ12M8: 4-node quadrilateral element with drilling DOFs and 8 internal parameters, Long et al. [35].
- Pimpinelli [39]: assumed strain quadrilateral element with drilling DOFs.
- D-type: 4-node quadrilateral element with drilling DOFs, Ibrahimovic et al. [32].
- Choi et al. [41]: 4-node hybrid Trefftz plane elasticity element with drilling DOFs.
- Choo et al. [42]: 4-node hybrid Trefftz plane elasticity element with drilling DOFs.
- Allman [53]: 4-node quadrilateral element with drilling DOFs.
- Allman [27]: 3-node triangular element with drilling DOFs.
- Zhang et al. [43]: 8-node quadrilateral element with drilling DOFs.

##### 4.1. Constant stress/stress problem

A small patch is divided into some arbitrary elements, as shown in Fig. 2. The displacement fields corresponding to the constant strain are:

$$u = 10^{-3}(x + y/2), \quad v = 10^{-3}(y + x/2), \quad \theta = 0. \quad (27)$$

The exact stress solution is as follows:

$$\sigma_x = \sigma_y = 1333.3333, \quad \tau_{xy} = 400.0 \quad (28)$$

The displacements of the boundary nodes are the displacement boundary conditions. No matter the inner element edges are straight or curved, and no matter the shapes of the elements are convex or concave, the exact results of the displacements and stresses at each node were obtained using the present HS-F element. This demonstrates that the new element passes the patch test and thus to ensure solution convergence.

4.2. Pure bending for a simply-supported beam (Fig. 3)

A simple beam with a length-to-height aspect ratio of 10 is subjected to a pure bending. There are exact solutions from the beam theory for the vertical displacement, the lateral displacement, and the end rotation. In all other literatures, this beam was usually modeled by one row of six regular or distorted membrane elements with drilling degrees of freedom (see mesh 5 and mesh 6 in Fig. 3). However, for the present element, i.e. HSF-Q4θ-7β, much

coarser meshes with distorted geometry are used: mesh 1 contains two regular elements; mesh 2 contains four degenerated triangles; mesh 3 also contains four distorted elements, with two of them degenerated into concave quadrangles; and mesh 4 contains four distorted elements similar to mesh 6. In addition to the simply-supported constraints, the drilling degree of freedom at point B (see Fig. 3) is restrained (i.e.  $\theta_B = 0$ ) due to symmetry. The displacement and stress results of select points are listed in Table 2.

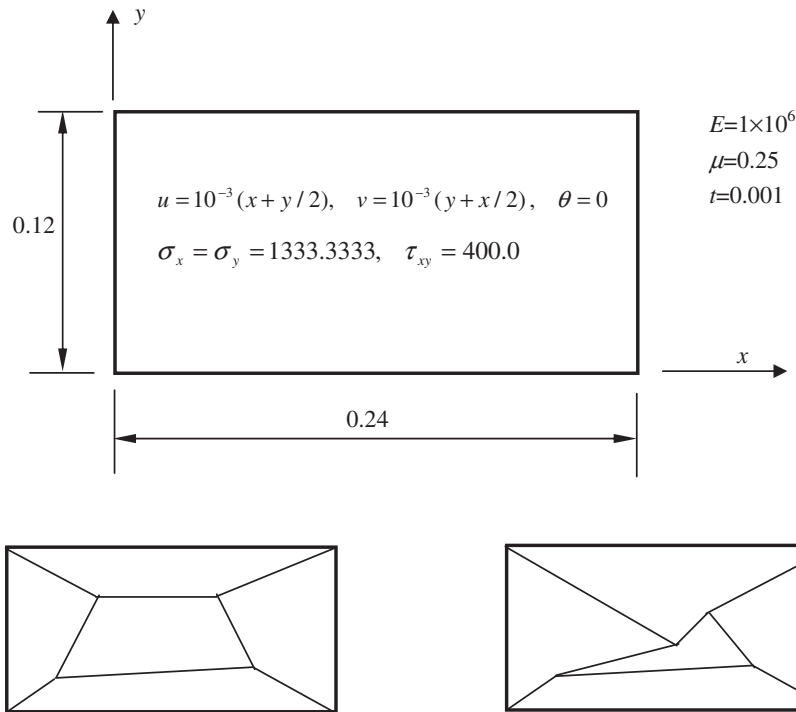


Fig. 2. Constant stress/strain patch test.

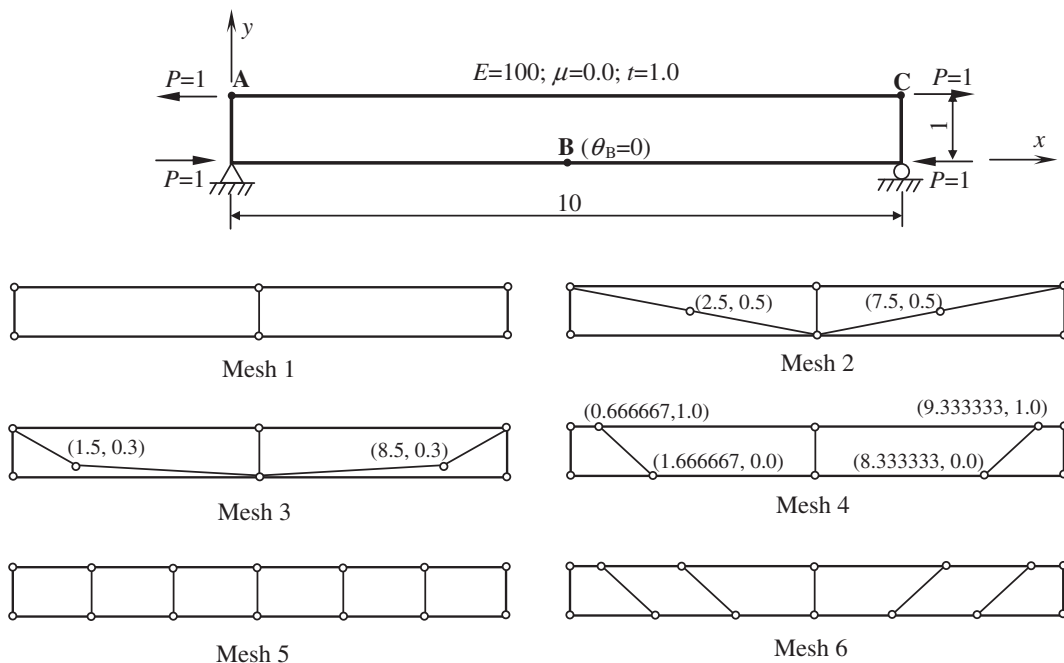


Fig. 3. Pure bending for a simply-supported beam.

**Table 2**  
Numerical results at selected points of a simply-supported cantilever under pure bending (Fig. 3).

| Model                            | Mesh   | $u_A$  | $v_B$ | $\theta_C$ | $\sigma_{xA}$ | $\sigma_{xB}$ | $\sigma_{xC}$ |
|----------------------------------|--------|--------|-------|------------|---------------|---------------|---------------|
| HSF-Q40-7 $\beta$                | Mesh 1 | -0.600 | 1.500 | -0.600     | 6.000         | -6.000        | 6.000         |
|                                  | Mesh 2 | -0.600 | 1.500 | -0.600     | 6.000         | -6.000        | 6.000         |
|                                  | Mesh 3 | -0.597 | 1.493 | -0.566     | 6.100         | -6.155        | 6.100         |
|                                  | Mesh 4 | -0.598 | 1.502 | -0.613     | 6.040         | -6.219        | 6.040         |
|                                  | Mesh 5 | -0.600 | 1.500 | -0.600     | 6.000         | -6.000        | 6.000         |
|                                  | Mesh 6 | -0.599 | 1.517 | -0.650     | 6.021         | -6.052        | 6.021         |
| Allman [27]                      | Mesh 5 | -0.600 | 1.500 | -0.600     | -             | -             | -             |
|                                  | Mesh 6 | -0.498 | 1.215 | -0.536     | -             | -             | -             |
| D-type [32]                      | Mesh 5 | -0.600 | 1.500 | -0.600     | -             | -             | -             |
|                                  | Mesh 6 | -      | 1.142 | -0.573     | -             | -             | -             |
| Pimpinelli [39]                  | Mesh 5 | -      | 1.500 | -0.600     | -             | -             | -             |
|                                  | Mesh 6 | -      | 1.390 | -0.540     | -             | -             | -             |
| Choi et al. [41]                 | Mesh 5 | -0.600 | 1.500 | -0.600     | -             | -             | -             |
|                                  | Mesh 6 | -0.599 | 1.517 | -0.632     | -             | -             | -             |
| Zhang et al. [43] (8-node model) | Mesh 5 | -      | 1.500 | -0.600     | -             | -             | -             |
|                                  | Mesh 6 | -      | 1.242 | -0.595     | -             | -             | -             |
| Exact                            |        | -0.600 | 1.500 | -0.600     | 6.000         | -6.000        | 6.000         |

It can be seen that the present element HSF-Q40-7 $\beta$  provides good results in all mesh divisions. It is quite insensitive to various mesh distortions, even when some quadrilateral elements degenerate to be triangles or concave quadrangles. Furthermore, even if the drilling degrees of freedom were not restrained, the same results can still be obtained for the vertical and lateral displacements, and the stresses as well.

#### 4.3. MacNeal's thin cantilever beam with distorted meshes (Fig. 4)

Consider a thin beam presented in Fig. 4. Three different mesh shapes are adopted: rectangular, parallelogram and trapezoidal. This example, proposed by MacNeal et al. [49], is a classic benchmark for testing the sensitivity to mesh distortion of 4-node quadrilateral membrane elements. Besides the distortion caused by the

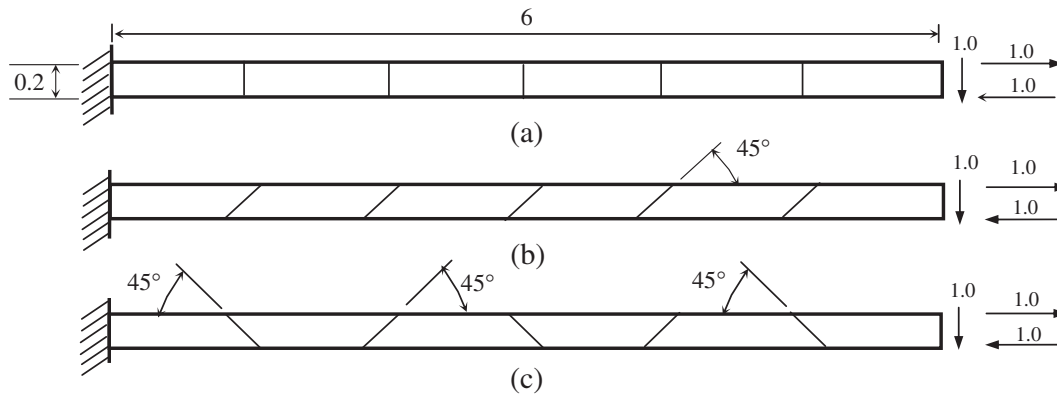


**Fig. 4.** MacNeal's beam problem.

**Table 3**  
The normalized results of the tip deflection for the MacNeal's thin beam using different meshes (Fig. 4).

| Element           | Load $P$ |                    |          | Load $M$ |                    |          |
|-------------------|----------|--------------------|----------|----------|--------------------|----------|
|                   | Mesh (a) | Mesh (b)           | Mesh (c) | Mesh (a) | Mesh (b)           | Mesh (c) |
| Q4                | 0.093    | 0.035              | 0.003    | 0.093    | 0.031              | 0.022    |
| QM6 [50]          | 0.993    | 0.623              | 0.044    | 1.000    | 0.722              | 0.037    |
| QUAD4 [49]        | 0.904    | 0.080              | 0.071    | -        | -                  | -        |
| P-S [51]          | 0.993    | 0.798              | 0.221    | 1.000    | 0.852              | 0.167    |
| Allman [53]       | 0.904    | 0.873              | 0.805    | 0.910    | -                  | -        |
| Q4S [30]          | 0.993    | 0.988              | 0.986    | -        | -                  | -        |
| GQ12M8 [35]       | 0.993    | 0.993              | 0.988    | -        | -                  | -        |
| Choi et al. [41]  | 0.993    | 0.988              | 0.985    | 1.000    | -                  | -        |
| HSF-Q40-7 $\beta$ | 0.993    | 0.988              | 0.991    | 1.000    | 0.996              | 0.999    |
| Exact             |          | 1.000 <sup>a</sup> |          |          | 1.000 <sup>b</sup> |          |

<sup>a</sup> The standard value is -0.1081.

<sup>b</sup> The standard value is -0.0054.

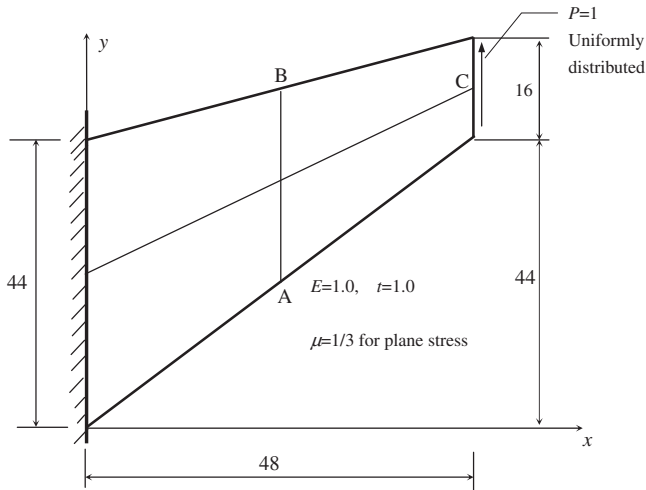


Fig. 5. Cook's skew beam problem.

length-width ratio, a combined distortions of parallelogram and trapezoidal shapes together with length-width ratio are taken into account.

There are two loading cases under consideration: bending and shearing at the free end, respectively. The Young's modulus of the beam is  $E = 10^7$ ; the Poisson's ratio,  $\mu = 0.3$ ; and the thickness of the beam,  $t = 0.1$ . The results of the tip deflection are shown in Table 3. In addition to the proposed element, the results obtained by well-known 4-node conventional isoparametric element, incompatible element, hybrid-stress element, and models with drilling degrees of freedom, are also given for comparison. It can be seen that the present element possesses the best accuracy.

4.4. Cook's skew beam problem (Fig. 5)

As shown in Fig. 5, a skew cantilever under plane stress condition is subjected to a shear distributed load at the free edge. This

example was proposed by Cook [52]. The results of vertical deflection at point C, the maximum principal stress at point A and the minimum principal stress at point B are all listed in Table 4. Compared with the results of other elements with drilling degrees of freedom, the present model exhibits better convergence property, especially for the stresses.

4.5. Cantilever beam subjected shearing at the free end (Fig. 6)

A cantilever beam is calculated by using five distorted and regular mesh divisions (see Fig. 6). The results of the tip deflections and stress  $\sigma_x$  at a selected point (12, 6) are listed in Table 5. From Table 5, it can be seen again that the element HSF-Q40-7 $\beta$  gives more accurate solutions than those obtained from other elements, also insensitive to mesh distortion.

4.6. A wedge subjected to a uniformly distributed load (Fig. 7)

As shown in Fig. 7, a cantilever wedge is subjected to a uniformly distributed load  $q$ . Because of its triangular shape, the wedge cannot be modeled without the use of triangular and/or distorted quadrilateral elements. The theoretical solutions for this problem are given by [54]

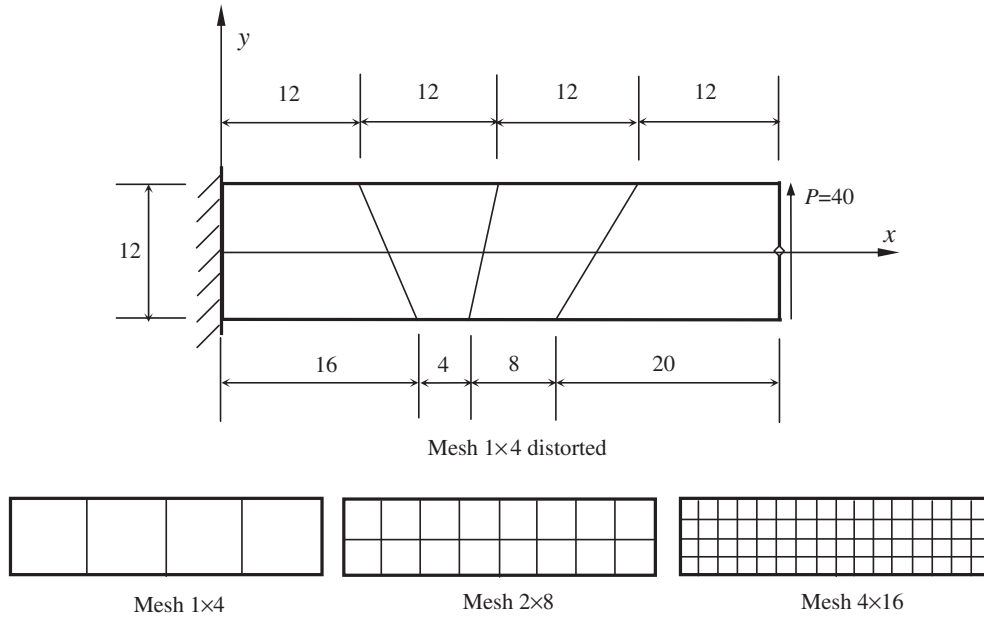
$$\left. \begin{aligned} \sigma_r &= \frac{q}{tg\alpha - \alpha} (\alpha - \theta - \sin\theta \cos\theta - \sin^2\theta tg\alpha), \\ \sigma_\theta &= \frac{q}{tg\alpha - \alpha} (\alpha - \theta + \sin\theta \cos\theta - \cos^2\theta tg\alpha), \\ \tau_{r\theta} &= \frac{q}{2(tg\alpha - \alpha)} (1 + \sin^2\theta - \cos^2\theta - 2tg\alpha \sin\theta \cos\theta). \end{aligned} \right\} \quad (29)$$

Since the present quadrilateral HS-F element can still perform well when its shape degenerates into triangle (Examples 4.1 and 4.2), it can therefore be readily used to model the wedge problem. As shown in Fig. 7, three mesh divisions,  $1 \times 6$ ,  $2 \times 12$  and  $4 \times 24$ , are employed, in which some elements are triangular in shape. Numerical results and the percentage errors of the radial stresses at selected points are listed in Table 6. Again, the present element HSF-Q40-7 $\beta$  performs very well for such high-order bending problem.

Table 4 Results of Cook's skew beam under plane stress condition (Fig. 5).

| Mesh density                       | Element                            | $u_c$       | $\sigma_{Amax}$ | $\sigma_{Bmin}$ |
|------------------------------------|------------------------------------|-------------|-----------------|-----------------|
| 2 × 2                              | Allman [53]                        | 20.27       | 0.1825          | -0.1716         |
|                                    | Q4S [30]                           | 21.27       | 0.1600          | -0.2307         |
|                                    | GQ12M8 [35]                        | 22.49       | 0.2083          | -0.2216         |
|                                    | Pimpinelli [39]                    | 21.02       | -               | -               |
|                                    | Zhang et al. [43] (8-node)         | 22.76       | 0.2145          | -0.1934         |
|                                    | Choi et al. [41]                   | 22.55       | 0.1721          | -0.2306         |
|                                    | <b>HSF-Q40-7<math>\beta</math></b> | 22.55       | 0.2158          | -0.2086         |
|                                    | 4 × 4                              | Allman [53] | 22.78           | 0.2261          |
| Q4S [30]                           |                                    | 23.06       | 0.2355          | -0.1516         |
| GQ12M8 [35]                        |                                    | 23.44       | 0.2338          | -0.2045         |
| Pimpinelli [39]                    |                                    | 23.01       | -               | -               |
| Zhang et al. [43] (8-node)         |                                    | 23.21       | 0.2238          | -0.1994         |
| Choi et al. [41]                   |                                    | 23.44       | 0.2181          | -0.1879         |
| <b>HSF-Q40-7<math>\beta</math></b> |                                    | 23.44       | 0.2357          | -0.2029         |
| 8 × 8                              |                                    | Allman [53] | 23.56           | 0.2340          |
|                                    | Q4S [30]                           | 23.66       | 0.2379          | -0.1803         |
|                                    | GQ12M8 [35]                        | 23.78       | 0.2361          | -0.2028         |
|                                    | Pimpinelli [39]                    | 23.68       | -               | -               |
|                                    | Zhang et al. [43] (8-node)         | 23.89       | 0.2352          | -0.2008         |
|                                    | Choi et al. [41]                   | 23.79       | 0.2303          | -0.1929         |
|                                    | <b>HSF-Q40-7<math>\beta</math></b> | 23.79       | 0.2364          | -0.2027         |
|                                    | 16 × 16                            | Q4S [30]    | 23.86           | 0.2383          |
| Choi et al. [41]                   |                                    | 23.90       | 0.2347          | -0.1982         |
| <b>HSF-Q40-7<math>\beta</math></b> |                                    | 23.90       | 0.2367          | -0.2039         |
| Reference solution <sup>a</sup>    |                                    | 23.96       | 0.2362          | -0.2023         |

<sup>a</sup> Results of the element GT9M8 [36] using  $64 \times 64$  mesh.



$E=30000.0$ ;  $\mu=0.25$ ;  $t=1.0$ ;  $P=40$

**Fig. 6.** Cantilever beam with various mesh divisions.

**Table 5**  
The tip deflection and normal stresses of cantilever beam (Fig. 6).

|                       | Mesh            | Allman [27] | Allman [53] | Pimpinelli [39] | Zhang et al. [43] (8-node model) | HSF-Q40-7 $\beta$ |
|-----------------------|-----------------|-------------|-------------|-----------------|----------------------------------|-------------------|
| $\delta_{tip}$        | 1 × 4 distorted | –           | –           | –               | –                                | 0.3506            |
|                       | 1 × 4           | 0.2696      | 0.3026      | 0.3493          | 0.3445                           | 0.3493            |
|                       | 2 × 8           | 0.3261      | 0.3394      | 0.3523          | 0.3505                           | 0.3541            |
|                       | 4 × 16          | 0.3471      | 0.3512      | 0.3548          | 0.3549                           | 0.3559            |
|                       | Exact [54]      | 0.3558      |             |                 |                                  |                   |
| $\sigma_x$ at (12, 6) | 1 × 4 distorted | –           | –           | –               | –                                | 59.081            |
|                       | 1 × 4           | 39.4        | 52.7        | –               | 55.3                             | 60.000            |
|                       | 2 × 8           | 52.3        | 58.4        | –               | 57.8                             | 60.510            |
|                       | 4 × 16          | 59.6        | 59.7        | –               | 59.9                             | 60.040            |
|                       | Exact [54]      | 60.000      |             |                 |                                  |                   |

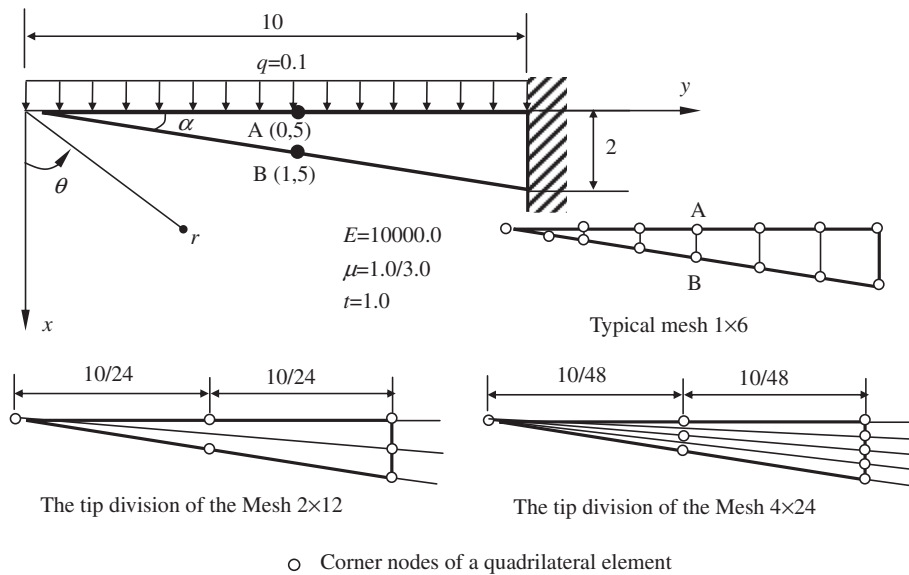


**Fig. 7.** A wedge subjected to a uniformly distributed load.

**Table 6**  
HSF-Q40-7β results of radial stress at selected points for a wedge subjected to a uniformly distributed load (Fig. 7).

| Mesh                         | 1 × 6           | 2 × 12          | 4 × 24          | Exact [54] |
|------------------------------|-----------------|-----------------|-----------------|------------|
| $\sigma_r$ at point A (0, 5) | 7.6835 (1.38%)  | 7.5894 (0.13%)  | 7.5806 (0.02%)  | 7.5792     |
| $\sigma_r$ at point B (1, 5) | -7.7920 (1.47%) | -7.7088 (0.39%) | -7.6832 (0.05%) | -7.6792    |

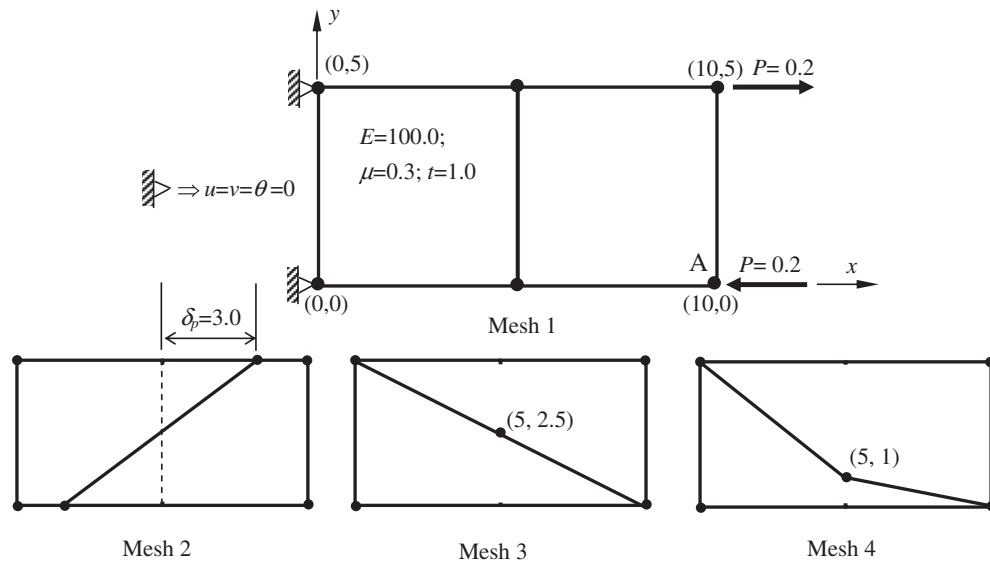


**Fig. 8.** Rotation dependence test: cantilever beam problem and meshes.

**Table 7**  
Percentage (%) error<sup>a</sup> of HSF-Q40-7β in the displacement at point A computed for the rotational frame invariance test (Fig. 8).

| $\theta$ | 0°                                    | 10°   | 20°   | 30°   | 40°   | 50°   | 60°   | 70°   | 80°   | 90°   |
|----------|---------------------------------------|-------|-------|-------|-------|-------|-------|-------|-------|-------|
| Mesh 1   | -0.62<br>(Numerical results: 0.05366) | -0.62 | -0.62 | -0.62 | -0.62 | -0.62 | -0.62 | -0.62 | -0.62 | -0.62 |
| Mesh 2   | -0.21<br>(Numerical results: 0.05389) | -0.21 | -0.21 | -0.21 | -0.21 | -0.21 | -0.21 | -0.21 | -0.21 | -0.21 |
| Mesh 3   | -0.62<br>(Numerical results: 0.05366) | -0.62 | -0.62 | -0.62 | -0.62 | -0.62 | -0.62 | -0.62 | -0.62 | -0.62 |
| Mesh 4   | -3.55<br>(Numerical results: 0.05208) | -3.55 | -3.55 | -3.55 | -3.55 | -3.55 | -3.55 | -3.55 | -3.55 | -3.55 |

<sup>a</sup> With respect to 'overkill' solution = 0.054.

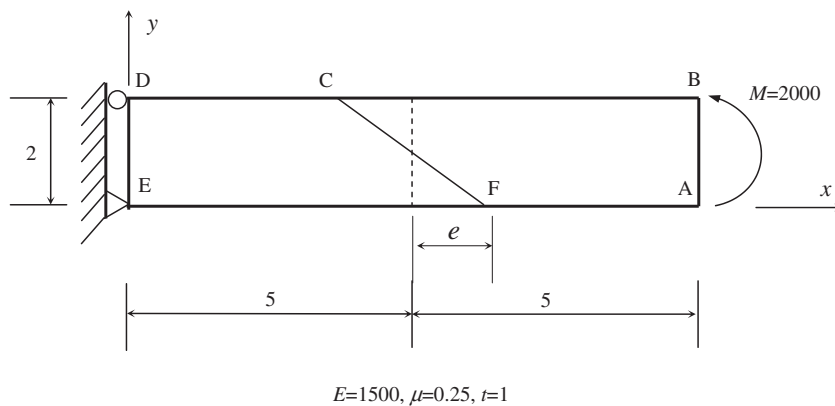


**Fig. 9.** Cantilever beam represented by two elements with distortion parameter  $e$ .

**Table 8**  
Results of the maximum displacements and stresses of a cantilever beam subjected to a pure bending  $M$  (Fig. 9).

| $e$                      | 0          | 0.5           | 1             | 2             | 3             | 4             | 4.9           | 5          | Exact |
|--------------------------|------------|---------------|---------------|---------------|---------------|---------------|---------------|------------|-------|
| $u_A$                    | 20         | 20            | 20            | 20            | 20            | 20            | 20            | 20         | 20    |
| $u_B$                    | -20        | -20           | -20           | -20           | -20           | -20           | -20           | -20        | -20   |
| $v_A$                    | <b>100</b> | <b>99.93</b>  | <b>99.47</b>  | <b>95.95</b>  | <b>87.14</b>  | <b>71.87</b>  | <b>52.47</b>  | <b>50</b>  | 100   |
| $v_B$                    | 100        | 100           | 100           | 100           | 100           | 100           | 100           | 100        | 100   |
| $v_B$ by Choo et al [41] | 100        | 99.2          | 99.6          | 100.9         | 83.6          | 57.8          | 41.4          | -          | 100   |
| $v_B$ by Allman [53]     | 93.8       | 95.0          | 90.7          | 56.7          | 31.8          | 17.9          | 11.2          | -          | 100   |
| $\sigma_{xA}$            | 3000       | 3000          | 3000          | 3000          | 3000          | 3000          | 3000          | 3000       | 3000  |
| $\sigma_{xB}$            | -3000      | -3000         | -3000         | -3000         | -3000         | -3000         | -3000         | -3000      | -3000 |
| $\sigma_{xC}$            | -3000      | -3000         | -3000         | -3000         | -3000         | -3000         | -3000         | -3000      | -3000 |
| $\sigma_{xD}$            | -3000      | -3000         | -3000         | -3000         | -3000         | -3000         | -3000         | -3000      | -3000 |
| $\sigma_{xE}$            | 3000       | 3000          | 3000          | 3000          | 3000          | 3000          | 3000          | 3000       | 3000  |
| $\sigma_{xF}$            | 3000       | 3000          | 3000          | 3000          | 3000          | 3000          | 3000          | 3000       | 3000  |
| $e$                      | 0          | -0.5          | -1            | -2            | -3            | -4            | -4.9          | -5         | Exact |
| $u_A$                    | 20         | 20            | 20            | 20            | 20            | 20            | 20            | 20         | 20    |
| $u_B$                    | -20        | -20           | -20           | -20           | -20           | -20           | -20           | -20        | -20   |
| $v_A$                    | <b>100</b> | <b>100.07</b> | <b>100.53</b> | <b>104.05</b> | <b>112.86</b> | <b>128.13</b> | <b>147.53</b> | <b>150</b> | 100   |
| $v_B$                    | 100        | 100           | 100           | 100           | 100           | 100           | 100           | 100        | 100   |
| $\sigma_{xA}$            | 3000       | 3000          | 3000          | 3000          | 3000          | 3000          | 3000          | 3000       | 3000  |
| $\sigma_{xB}$            | -3000      | -3000         | -3000         | -3000         | -3000         | -3000         | -3000         | -3000      | -3000 |
| $\sigma_{xC}$            | -3000      | -3000         | -3000         | -3000         | -3000         | -3000         | -3000         | -3000      | -3000 |
| $\sigma_{xD}$            | -3000      | -3000         | -3000         | -3000         | -3000         | -3000         | -3000         | -3000      | -3000 |
| $\sigma_{xE}$            | 3000       | 3000          | 3000          | 3000          | 3000          | 3000          | 3000          | 3000       | 3000  |
| $\sigma_{xF}$            | 3000       | 3000          | 3000          | 3000          | 3000          | 3000          | 3000          | 3000       | 3000  |

#### 4.7. Rotational frame dependence test (Fig. 8)

In order to show that there is no rotational frame dependence for the present element model, a benchmark previously tested by Spilker et al. [55] is considered. As shown in Fig. 8, a cantilever beam is rotated counterclockwise from  $0^\circ$  to  $90^\circ$  in steps of  $10^\circ$ , and the problem is solved for the displacements at each step. The magnitude of displacement, i.e.,  $\sqrt{u^2 + v^2}$  at point A is monitored to study the rotational frame-dependent behavior. The test is then repeated using the four types of meshes, as shown in Fig. 8.

Table 7 shows the results and the percentage errors. The magnitude of displacements, based on an 'overkill' finite element model composed of 20,000 8-node quadrilateral elements, were obtained using ABAQUS as a reference solution. It can be seen that the present model HSF-Q40-7 $\beta$  provides invariance under coordinate rotations.

#### 4.8. Cantilever beam represented by two elements containing a parameter of distortion (Fig. 9)

The cantilever beam shown in Fig. 9 is meshed into two elements. The shape of the two elements varies with a distortion parameter  $e$ . When  $e = 0$ , both elements are rectangular. With the increase or decrease of  $e$  value, the mesh is distorted more and more severely. This is a well-known benchmark for testing the sensitivity to mesh distortion.

For the case of pure bending problems (load  $M$ ), the results of the maximum displacements, including the vertical and lateral displacements at the tip points A and B, are listed in Table 8. Meanwhile, the results of the maximum stress  $\sigma_x$  at points A, B, C, D, E and F are also given, in which C and F are two moving points. From Table 7, it is surprising that most results (especially, all the stress values) kept to be exact values during the entire distortion process, even when two adjacent nodes are in coincidence. Only the deflection at point A is affected by the distortion, but it is still in an acceptable range.

## 5. Concluding remarks

In the present paper, a new 4-node quadrilateral plane hybrid stress-function (HS-F) element, with drilling degrees of freedom

has been formulated and tested numerically. The element exhibits the following attributes:

- (i) The theoretical basis of the present hybrid stress-function (HS-F) is the principle of minimum complementary energy, which has been seldom used for development of other popular finite element models. The value of this principle for formulating a high performance finite element model is revealed again in the paper. In the proposed derivation, only assumed internal stress fields and boundary displacements are needed, which is much easier to achieve.
- (ii) Differing from the traditional schemes, the element stress fields are derived from the first seven fundamental analytical solutions (in global Cartesian coordinates) of the Airy stress function, and the stresses so obtained satisfy both the equilibrium and compatibility relations. Besides, the resulting function possesses the first-order completeness in Cartesian coordinates.
- (iii) The new element exhibits better performance in both displacement and stress solutions. Furthermore, it is useful to mention that the proposed element is quite insensitive to severe mesh distortion. It still performs quite well even when the element shape degenerates into a triangle or concave quadrangle.
- (iv) The proposed element has a stiffness matrix similar in form as those of displacement-based elements, thus it can be readily incorporated into a standard finite element program framework.

Compared with other numerous displacement-based formulations, such as the modified incompatible mode method [19], which can also successfully deal with the element distortion, the most valuable advantage of the proposed formulations is that, they can well handle more severe distortion cases. Since there is no Jacobi inverse existing in all integration formulae (Eqs. (14) and (17)), the influence caused by the element shape becomes very small. So, the new element can still perform well even when the shape of a convex quadrilateral element degenerates into triangle or concave quadrangle, which cannot be handled well by the usual formulations. Furthermore, the accuracy for stress solutions obtained by the present element is obviously higher than those

by the usual displacement-based formulations with the same order.

Some finite element techniques, including the incompatible mode formulation, can be generalized to other problems of interest, such as plates, shells and 3D solids with rotational degrees of freedom [20,21]. Actually, once the sufficient fundamental solutions for the stress functions, or the stresses simultaneously satisfying both the equilibrium and compatibility equations, are found, the corresponding element models can be established by following the procedure proposed in this work. To-date, the appropriate fundamental stress solutions for fracture, 3D and Mindlin–Reissner plate problems have been already obtained. And these works will be reported in other future papers.

However, unlike the incompatible mode method for displacement-based models, which has been applied for efficient analysis of nonlinear problems for either material or geometric nonlinearities [22–26], the proposed formulations may be more difficult and inefficient to be used in these fields. But, some successful applications of hybrid-stress elements in nonlinear problems have been presented by some researchers [56]. These experiences could be used for reference in further studies.

### Acknowledgements

We thank Prof. Paul T.Y. Chang for helping us improve written English of this paper and giving us many good suggestions. This study was supported by the Natural Science Foundation of China (Project Nos. 10872108, 10876100), the Program for New Century Excellent Talents in University (Project No. NCET-07-0477), the National Basic Research Program of China (Project No. 2010CB832701), and the Astronautic Science Foundation of China (ASFC).

### Appendix

The evaluation procedure of symmetrical matrix **M** in Eq. (14)

In order to evaluate the matrix **M** by numerical integration, the Cartesian coordinates should be expressed in terms of local coordinates (isoparametric coordinates). Let

$$x = \sum_{i=1}^4 N_i^0(\xi, \eta) x_i, \quad y = \sum_{i=1}^4 N_i^0(\xi, \eta) y_i, \quad (A1)$$

where  $(x_i, y_i)$  ( $i = 1-4$ ) are the Cartesian coordinates of the node  $i$ ;  $N_i^0(\xi, \eta)$  ( $i = 1-4$ ) are the shape functions of the standard 4-node Serendipity isoparametric elements.

Then, after substituting Eq. (A1) into Eq. (15), matrix **S** becomes

$$\mathbf{S}(x, y) = \mathbf{S}(\xi, \eta). \quad (A2)$$

Thus, Eq. (14) can be rewritten as

$$\mathbf{M} = \int_{-1}^1 \int_{-1}^1 \mathbf{S}(\xi, \eta)^T \mathbf{C} \mathbf{S}(\xi, \eta) t \mathbf{J} |d\xi d\eta, \quad (A3)$$

where **J** is the Jacobian determinant. Then, a Gauss integration scheme can be used for evaluation of Eq. (A3). The numbers of Gauss points are  $2 \times 2$ .

The evaluation procedure of matrix **H** in Eq. (17)

The evaluation of Eq. (17) should be performed along four element edges. So Eq. (17) can be rewritten as

$$\mathbf{H} = \int_{\Gamma_{12}} \mathbf{S}^T \mathbf{L}^T \bar{\mathbf{N}} t ds + \int_{\Gamma_{23}} \mathbf{S}^T \mathbf{L}^T \bar{\mathbf{N}} t ds + \int_{\Gamma_{34}} \mathbf{S}^T \mathbf{L}^T \bar{\mathbf{N}} t ds + \int_{\Gamma_{41}} \mathbf{S}^T \mathbf{L}^T \bar{\mathbf{N}} t ds, \quad (A4)$$

where  $\Gamma_{12}$ ,  $\Gamma_{23}$ ,  $\Gamma_{34}$  and  $\Gamma_{41}$  denote element edges  $\bar{12}$ ,  $\bar{23}$ ,  $\bar{34}$  and  $\bar{41}$ , respectively.

The direction cosines of the outer normal of each element edge,  $l$  and  $m$  in Eq. (6), are given by

$$l = \frac{dy}{ds}, \quad m = -\frac{dx}{ds}. \quad (A5)$$

Along edges  $\bar{12}$  ( $\eta = -1$ ) and  $\bar{34}$  ( $\eta = 1$ ), the relations between  $ds$  and  $d\xi$  are given by

$$ds = \left[ \left( \frac{dx}{d\xi} \right)^2 + \left( \frac{dy}{d\xi} \right)^2 \right]_{\eta=-1}^{1/2} d\xi, \quad ds = - \left[ \left( \frac{dx}{d\xi} \right)^2 + \left( \frac{dy}{d\xi} \right)^2 \right]_{\eta=1}^{1/2} d\xi; \quad (A6)$$

and along edge  $\bar{23}$  ( $\xi = 1$ ) and  $\bar{41}$  ( $\xi = -1$ ), the relations between  $ds$  and  $d\eta$  are given by

$$ds = \left[ \left( \frac{dx}{d\eta} \right)^2 + \left( \frac{dy}{d\eta} \right)^2 \right]_{\xi=1}^{1/2} d\eta, \quad ds = - \left[ \left( \frac{dx}{d\eta} \right)^2 + \left( \frac{dy}{d\eta} \right)^2 \right]_{\xi=-1}^{1/2} d\eta. \quad (A7)$$

Thus, substitution of Eqs. (A1), (A2), (26), (A5), (A6), (A7) into Eq. (A4) yields

$$\mathbf{H} = \int_{-1}^1 \mathbf{S}(\xi, -1)^T \tilde{\mathbf{L}}_{|\eta=-1}^T \bar{\mathbf{N}}_{|\eta=-1} t d\xi + \int_{-1}^1 \mathbf{S}(1, \eta)^T \tilde{\mathbf{L}}_{|\xi=1}^T \bar{\mathbf{N}}_{|\xi=1} t d\eta - \int_{-1}^1 \mathbf{S}(\xi, 1)^T \tilde{\mathbf{L}}_{|\eta=1}^T \bar{\mathbf{N}}_{|\eta=1} t d\xi - \int_{-1}^1 \mathbf{S}(-1, \eta)^T \tilde{\mathbf{L}}_{|\xi=-1}^T \bar{\mathbf{N}}_{|\xi=-1} t d\eta, \quad (A8)$$

where

$$\tilde{\mathbf{L}}_{|\eta=-1} = \begin{bmatrix} \frac{dy}{d\xi} & 0 & -\frac{dx}{d\xi} \\ 0 & -\frac{dx}{d\xi} & \frac{dy}{d\xi} \end{bmatrix}_{\eta=-1} = \begin{bmatrix} \sum_{i=1}^4 \frac{dN_i^0}{d\xi} y_i & 0 & -\sum_{i=1}^4 \frac{dN_i^0}{d\xi} x_i \\ 0 & -\sum_{i=1}^4 \frac{dN_i^0}{d\xi} x_i & \sum_{i=1}^4 \frac{dN_i^0}{d\xi} y_i \end{bmatrix}_{\eta=-1}, \quad (A9a)$$

$$\tilde{\mathbf{L}}_{|\xi=1} = \begin{bmatrix} \frac{dy}{d\eta} & 0 & -\frac{dx}{d\eta} \\ 0 & -\frac{dx}{d\eta} & \frac{dy}{d\eta} \end{bmatrix}_{\xi=1} = \begin{bmatrix} \sum_{i=1}^4 \frac{dN_i^0}{d\eta} y_i & 0 & -\sum_{i=1}^4 \frac{dN_i^0}{d\eta} x_i \\ 0 & -\sum_{i=1}^4 \frac{dN_i^0}{d\eta} x_i & \sum_{i=1}^4 \frac{dN_i^0}{d\eta} y_i \end{bmatrix}_{\xi=1}, \quad (A9b)$$

$$\tilde{\mathbf{L}}_{|\eta=1} = \begin{bmatrix} \frac{dy}{d\xi} & 0 & -\frac{dx}{d\xi} \\ 0 & -\frac{dx}{d\xi} & \frac{dy}{d\xi} \end{bmatrix}_{\eta=1} = \begin{bmatrix} \sum_{i=1}^4 \frac{dN_i^0}{d\xi} y_i & 0 & -\sum_{i=1}^4 \frac{dN_i^0}{d\xi} x_i \\ 0 & -\sum_{i=1}^4 \frac{dN_i^0}{d\xi} x_i & \sum_{i=1}^4 \frac{dN_i^0}{d\xi} y_i \end{bmatrix}_{\eta=1}, \quad (A9c)$$

$$\tilde{\mathbf{L}}_{|\xi=-1} = \begin{bmatrix} \frac{dy}{d\eta} & 0 & -\frac{dx}{d\eta} \\ 0 & -\frac{dx}{d\eta} & \frac{dy}{d\eta} \end{bmatrix}_{\xi=-1} = \begin{bmatrix} \sum_{i=1}^4 \frac{dN_i^0}{d\eta} y_i & 0 & -\sum_{i=1}^4 \frac{dN_i^0}{d\eta} x_i \\ 0 & -\sum_{i=1}^4 \frac{dN_i^0}{d\eta} x_i & \sum_{i=1}^4 \frac{dN_i^0}{d\eta} y_i \end{bmatrix}_{\xi=-1}. \quad (A9d)$$

Two Gauss integration points are theoretically needed for evaluating Eq. (A8).

## References

- [1] Lee NS, Bathe KJ. Effects of element distortion on the performance of isoparametric elements. *Int J Numer Methods Eng* 1993;36:3553–76.
- [2] Bathe KJ. *Finite element procedures*. Englewood Cliffs, NJ: Prentice Hall; 1996.
- [3] Long YQ, Cen S, Long ZF. *Advanced finite element method in structural engineering*. Springer-Verlag GmbH, Tsinghua University Press: Berlin, Heidelberg, Beijing; 2009.
- [4] Long YQ, Li JX, Long ZF, Cen S. Area coordinates used in quadrilateral elements. *Commun Numer Methods Eng* 1999;15(8):533–45.
- [5] Long ZF, Li JX, Cen S, Long YQ. Some basic formulae for area coordinates used in quadrilateral elements. *Commun Numer Methods Eng* 1999;15(12):841–52.
- [6] Chen XM, Cen S, Long YQ, Yao ZH. Membrane elements insensitive to distortion using the quadrilateral area coordinate method. *Comput Struct* 2004;82(1):35–54.
- [7] Cen S, Chen XM, Fu XR. Quadrilateral membrane element family formulated by the quadrilateral area coordinate method. *Comput Methods Appl Mech Eng* 2007;196(41–44):4337–53.
- [8] Chen XM, Cen S, Fu XR, Long YQ. A new quadrilateral area coordinate method (QACM-II) for developing quadrilateral finite element models. *Int J Numer Methods Eng* 2008;73(13):1911–41.
- [9] Cen S, Chen XM, Li CF, Fu XR. Quadrilateral membrane elements with analytical element stiffness matrices formulated by the new quadrilateral area coordinate method (QACM-II). *Int J Numer Methods Eng* 2009;77(8):1172–200.
- [10] Long ZF, Cen S, Wang L, Fu XR, Long YQ. The third form of the quadrilateral area coordinate method (QACM-III): theory, application, and scheme of composite coordinate interpolation. *Finite Elem Anal Des* 2010;46(10):805–18.
- [11] Li HG, Cen S, Cen ZZ. Hexahedral volume coordinate method (HVCM) and improvements on 3D Wilson hexahedral element. *Comput Methods Appl Mech Eng* 2008;197(51–52):4531–48.
- [12] Rajendran S, Liew KM. A novel unsymmetric 8-node plane element immune to mesh distortion under a quadratic displacement field. *Int J Numer Methods Eng* 2003;58:1713–48.
- [13] Rajendran S. A technique to develop mesh-distortion immune finite elements. *Comput Methods Appl Mech Eng* 2010;199(17–20):1044–63.
- [14] Ooi ET, Rajendran S, Yeo JH. A 20-node hexahedron element with enhanced distortion tolerance. *Int J Numer Methods Eng* 2004;60:2501–30.
- [15] Ooi ET, Rajendran S, Yeo JH. Remedies to rotational frame dependence and interpolation failure of US-QUAD8 element. *Commun Numer Methods Eng* 2008;24(11):1203–17.
- [16] Chen J, Li CJ, Chen WJ. A family of spline finite elements. *Comput Struct* 2010;88(11–12):718–27.
- [17] Chen J, Li CJ, Chen WJ. A 17-node quadrilateral spline finite element using the triangular area coordinates. *Appl Math Mech* 2010;31(1):125–34.
- [18] Liu GR, Nguyen-Thoi T, Lam KY. A novel FEM by scaling the gradient of strains with factor  $\alpha$  ( $\alpha$  FEM). *Comput Mech* 2009;43:369–91.
- [19] Ibrahimbegovic A, Wilson EL. A modified method of incompatible modes. *Commun Appl Numer Methods* 1991;7:187–94.
- [20] Ibrahimbegovic A, Wilson EL. Thick shell and solid finite elements with independent rotation fields. *Int J Numer Methods Eng* 1991;31:1393–414.
- [21] Ibrahimbegovic A. Plate quadrilateral finite element with incompatible modes. *Commun Appl Numer Methods* 1992;8:497–504.
- [22] Ibrahimbegovic A, Frey F. Stress resultant finite element analysis of reinforced concrete plates. *Eng Comput* 1993;10(1):15–30.
- [23] Ibrahimbegovic A, Frey F. An efficient implementation of stress resultant plasticity in analysis of Reissner–Mindlin plates. *Int J Numer Methods Eng* 1993;36:301–22.
- [24] Ibrahimbegovic A, Frey F. Geometrically nonlinear method of incompatible modes in application to finite elasticity with independent rotation field. *Int J Numer Methods Eng* 1993;36:4185–200.
- [25] Ibrahimbegovic A. On FE implementation of geometrically nonlinear Reissner's beam theory: three-dimensional curved beam elements. *Comput Methods Appl Mech Eng* 1995;122:11–26.
- [26] Ibrahimbegovic A, Kozar I. Nonlinear Wilson's brick element for finite elastic deformation of three-dimensional solids. *Commun Numer Methods Eng* 1995;11:655–64.
- [27] Allman DJ. A compatible triangular element including vertex rotations for plane elasticity analysis. *Comput Struct* 1984;19:1–8.
- [28] Bergan PG, Fellipa CA. A triangular membrane element with rotational degrees of freedom. *Comput Methods Appl Mech Eng* 1985;50:25–69.
- [29] Cook RD. A plane hybrid element with rotational D.O.F. and adjustable stiffness. *Int J Numer Methods Eng* 1987;24:1499–508.
- [30] MacNeal RH, Harder RL. A refined four-noded membrane element with rotational degrees of freedom. *Comput Struct* 1988;28:75–84.
- [31] Hughes TJR, Brezzi F. On drilling degrees of freedom. *Comput Methods Appl Mech Eng* 1989;72:105–21.
- [32] Ibrahimbegovic A, Taylor RL, Wilson EL. A robust quadrilateral membrane finite element with drilling degrees of freedom. *Int J Numer Methods Eng* 1990;30:445–57.
- [33] Iura M, Atluri SN. Formulation of a membrane finite element with drilling degrees of freedom. *Comput Mech* 1992;9:417–28.
- [34] Cazzani A, Atluri SN. Four-noded mixed finite elements, using unsymmetric stresses, for linear analysis of membranes. *Comput Mech* 1993;11:229–51.
- [35] Long YQ, Xu Y. Generalized conforming quadrilateral membrane element with vertex rigid rotational freedom. *Comput Struct* 1994;52(4):749–55.
- [36] Long YQ, Xu Y. Generalized conforming triangular membrane element with vertex rigid rotation al freedom. *Finite Elem Anal Des* 1994;17:259–71.
- [37] Piltner R, Taylor RL. Triangular finite elements with rotational degrees of freedom and enhanced strain modes. *Comput Struct* 2000;75:361–8.
- [38] Geyer S, Groenwold AA. Two hybrid stress membrane finite element families with drilling rotations. *Int J Numer Methods Eng* 2002;53:583–601.
- [39] Pimpinelli G. An assumed strain quadrilateral element with drilling degrees of freedom. *Finite Elem Anal Des* 2004;41:267–83.
- [40] Groenwold AA, Xiao QZ, Theron NJ. Accurate solution of traction free boundaries using hybrid stress membrane elements with drilling degrees of freedom. *Comput Struct* 2004;82:2071–81.
- [41] Choi N, Choo YS, Lee BC. A hybrid Trefftz plane elasticity element with drilling degrees of freedom. *Comput Methods Appl Mech Eng* 2006;195:4095–105.
- [42] Choo YS, Choi N, Lee BC. Quadrilateral and triangular plane elements with rotational degrees of freedom based on the hybrid Trefftz method. *Finite Elem Anal Des* 2006;42:1002–8.
- [43] Zhang H, Kuang JS. Eight-node membrane element with drilling degrees of freedom for analysis of in-plane stiffness of thick floor plates. *Int J Numer Methods Eng* 2008;76:2117–36.
- [44] Kugler S, Fotiu PA, Murin J. A highly efficient membrane finite element with drilling degrees of freedom. *Acta Mech* 2010;213(3–4):323–48.
- [45] Karaköse ÜHÇ, Askes H. Static and dynamic convergence studies of a four-noded membrane finite element with rotational degrees of freedom based on displacement superposition. *Int J Numer Methods Biomed Eng* 2010;26(10):1263–75.
- [46] Pian THH. Derivation of element stiffness matrices by assumed stress distributions. *AIAA J* 1964;2(7):1333–6.
- [47] Fu XR, Cen S, Li CF, Chen XM. Analytical trial function method for development of new 8-node plane element based on the variational principle containing airy stress function. *Eng Comput* 2010;27(4):442–63.
- [48] Cen S, Fu XR, Zhou MJ. A novel hybrid stress-function finite element method immune to severe mesh distortion. In: IOP Conference Series: Materials Science and Engineering (Proceedings of the WCCM/APCOM 2010), vol. 10; 2010. p. 012220.
- [49] MacNeal RH, Harder RL. A proposed standard set of problems to test finite element accuracy. *Finite Elem Anal Des* 1985;1(1):3–20.
- [50] Taylor RL, Beresford PJ, Wilson EL. A non-conforming element for stress analysis. *Int J Numer Methods Eng* 1976;10:1211–9.
- [51] Pian THH, Sumihara K. Rational approach for assumed stress finite elements. *Int J Numer Methods Eng* 1984;20:1685–95.
- [52] Cook RD, Malkus DS, Plesha ME. *Concepts and applications of finite element analysis*. 3rd ed. New York: John Wiley & Sons Inc.; 1989.
- [53] Allman DJ. A quadrilateral finite element including vertex rotations for plane elasticity analysis. *Int J Numer Methods Eng* 1988;26:717–30.
- [54] Timoshenko S, Goodier JN. *Theory of elasticity*. 3rd ed. New York: McGraw-Hill; 1979.
- [55] Spilker RL, Maskeri SM, Kania E. Plane isoparametric hybrid-stress elements: invariance and optimal sampling. *Int J Numer Methods Eng* 1981;17:1469–96.
- [56] Sze KY, Chan WK, Pian THH. An eight-node hybrid-stress solid-shell element for geometric non-linear analysis of elastic shells. *Int J Numer Methods Eng* 2002;55(7):853–78.